

MICRO-SYSTEM DISPLACEMENT AND PROFILE MEASUREMENT BY AN INTEGRATED PHOTON TUNNELING AND CONFOCAL MICROSCOPE

Wen-Jong Chen *

Institute of Mechanical Engineering

Chih-Kung Lee **

Institute of Applied Mechanics

Shui-Shong Lu **

Institute of Mechanical Engineering

Long-Sun Huang ***

Institute of Applied Mechanics

Ta-Shun Chu ****

Institute of Applied Mechanics

Ying-Chou Cheng *

Institute of Mechanical Engineering

Wu-Fone Yeh ****

Institute of Applied Mechanics

*National Taiwan University
Taipei, Taiwan 10617, R.O.C.*

ABSTRACT

An integrated optical method for measuring deformation of micro-mechanical systems with better than sub-micron resolutions is detailed. Both a confocal laser scanning microscope and a photon tunneling microscope were integrated into a single microscopy system due to their complimentary capabilities for examining sub-micrometer deformations. A halogen lamp and laser were adopted as the two light sources for the measurements. Since topographic information of samples up to a $15\mu\text{m}$ by $15\mu\text{m}$ area can be measured, a three-dimensional displacement field of the sample was extracted by comparing topographies of the same specimen area before and after deformation. The bending and twisting deformation of a micro-mirror driven by the electrostatic force was measured to demonstrate the capability of this newly developed instrument. The experimental data obtained agrees reasonably well with the theoretical results calculated by adopting an analytical solution and a finite element method. The small discrepancy in the result can be traced to the surface roughness effect, which is often non-negligible in micro-systems.

Keywords : Photon tunneling, Confocal, Topographic information.

1. INTRODUCTION

Parameters related to the mechanical performance of micro-electro-mechanical systems are important in determining the overall performance in this class of increasing important systems. Mechanical micro-mirrors, connected as light-modulator arrays [1,2], have been widely used in torsional actuators, projection display systems, scanners, and laser printers. A principal parameter for evaluating micro-mirrors is to analyze the angular rotation induced by the pull-in voltage between the mirror and electrodes. In order to acquire high performance and efficiency in different optical applications, many types of silicon-based micro-mirrors have been developed [3~5]. In recent years, the pull-in analysis that computes the angular rotation caused by the pull-in voltage has been

extensively researched [6,7]. One of the methods utilized adopts a parallel-plate model together with a torque coefficient of the device for estimating the relation between the angular rotation and the pull-in voltage [8]. A more complete and proper approach involves the use of a finite-elements model to predict the characteristics of a micro-mirror structure [9]. However, all these methods are mainly devoted to simulation methods for angular rotation estimations. In actual applications, a simple and rapid method to determine the angular rotation of the micro-mirror would be more effective in evaluating the characteristics and performance of the micro-mirror. A simple method based on optical triangulation was adopted [10,11], which focuses a laser beam onto a micro-mirror and then grabs the reflected beam by using a position sensitive photodetector. As the angular displacement of the micro-mirror was measured by the

* Ph.D. student

** Professor

*** Assistant Professor

**** Graduate student

differential voltage output of the detector, this particular method is sensitive to air and environmental turbulence. In addition, the optical structure between the micro-mirror and the detector must be accurately calibrated in order to quantify the rotational angle precisely.

In this paper, an alternative method developed for measuring angular rotation of micro-systems will be presented herein. That is, integrating a confocal laser scanning microscope (CLSM) and photon tunneling microscope (PTM) to arrive at the sub-micrometer measurement resolution required as both CLSM and PTM possess complimentary measurement resolutions and dynamic ranges. In addition, they have been widely used in measuring precision linear displacement in areas such as semiconductor and biomedical applications due to their sub-micrometer and even nanometer resolutions. The design concept and implementation of this newly developed integrated microscope, which switches between the CLSM and the PTM function by simply rotating its turret and turning on some subsystems, will be detailed in this paper.

The confocal microscope and PTM have been developed independently for the last 40 years [12,13]. The confocal microscope can use either a laser or a white-light source as its illumination source. The basis of its fundamental principle is that images of objects located slightly off the focused plane can be blocked by placing a pinhole at the image plane that is conjugated to the object plane of interest. The depth resolution achievable is in the range of sub-micrometers even though it actually depends on the magnification ratio and the corresponding pinhole used [12]. Since PTM achieves its depth resolution by using evanescent waves generated from the interface of a total internal reflection surface, i.e. the photon tunneling effect, its depth resolution is in the range of an unprecedented 0.01 angstroms [13]. Since optical techniques must make compromises to handle the tradeoff between dynamic range and resolution, it seems natural to integrate these two methods for micro-mechanical systems as the depth of focus and resolution are complimentary.

As detailed designs and their variants for different optical microscopes can be easily located in the literature, only the specific design adopted in this research which facilitates the smooth integration of CLSM and PTM will be discussed herein.

2. OVERALL SYSTEM REQUIREMENTS AND INSTRUMENTATION

The system design that matches the overall system requirement will be examined in this section. In addition, the fundamental principles of both CLSM and PTM will be briefly reviewed to see how these two methods can be integrated into a single system and to make sure the complimentary capabilities can be properly retained.

2.1 Experimental apparatus and procedures

A conventional BX 40 Olympus optical microscope was used as the base to integrate the CLSM and PTM (Fig. 1). The configurations for CLSM and PTM were chosen to make sure that these two newly designed systems could share the majority of the components. It is clear from Fig. 1 that if the halogen lamp is turned off in Section 2 and the beamsplitter 2 in the Double Port Tube Device is put into the optical path, the system can be set to operate in the CLSM mode. The laser light source is collimated in Section 1 and gets focused on the sample through the tube lens, beam splitter 2, the objective lens, and the reflected light is then collected by the detector in Section 3. In comparison, turning off the laser light source in Section 1 and turning on the halogen lamp leads to the PTM system operational mode. The reflected light from the sample surface passes through the tube lens and is captured by the CCD. The two subsystems will be described in detail later. Standard commercially available components were adopted to build the majority of the overall system in order to facilitate an easy and flexible implementation of different microscope modules. With this design concept in mind, only the opto-mechanical components needed to integrate multiple modules together were designed and custom-built to specifications. A 5 mW diode laser and a 50 W halogen lamp were used for the CLSM and PTM respectively as the light sources. A XYZ stage was used to translate the sample for 3D image construction. The returning light beam was collected by an Olympus microscope objective lens. Simply switching the different sub-systems result in automatically switching between the CLSM and the PTM functions. The surface information obtained from the CLSM was detected by a photo-detector and the evanescent wave induced image from the PTM was grabbed by using a charge-coupled device (CCD) camera. Both image information were digitized and then displayed on the computer screen. To minimize the influence of external disturbance during the experiments, the whole system was placed on a vibration isolation table.

2.2 Theory of confocal microscope

In the confocal scanning microscope configuration implemented, a diode laser was used as the light source and the confocal lens system was integrated with a simple stage to pursue image scanning with the point detection algorithm adopted (Fig. 1). The 5mW diode laser light source passed through a 25 μ m pinhole spatial filter and a 20mm diameter collimating lens to arrive at the microscope objective lens. The light beam was then focused by a 100x magnification objective lens of a 3mm working-distance to a single spot on the sample in order to satisfy the point illumination criterion. The light beam reflected from the sample surface passed back through the objective lens and was deflected by a 50% reflection/transmission ratio beamsplitter of 12.5mm

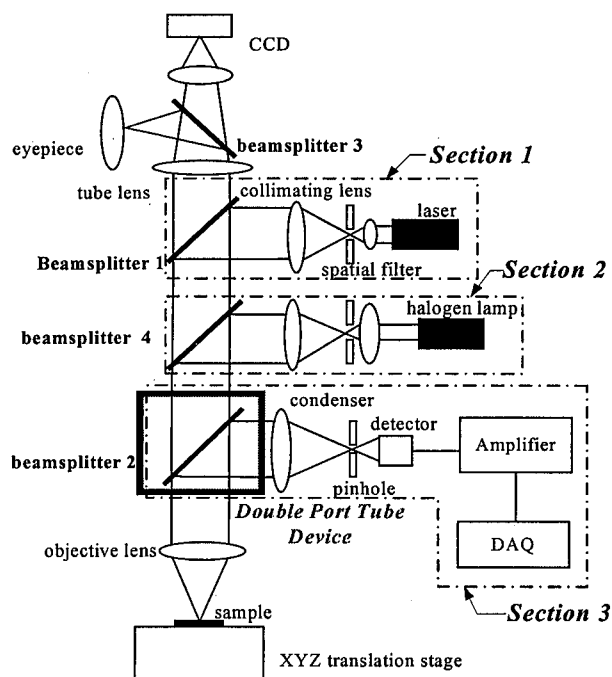


Fig. 1 Schematic of the integrated system

by 12.5mm size into the microscope, the second 100 \times magnification objective lens at NA = 0.8 and a 3mm working distance, focused the light beam onto a pinhole and the point detector. The full three-dimensional images were built-up point by point with the scanning stage traversing along the x-y raster pattern and the optical sectioning was done with the translation of the z-stage. That is, the optical sectioning was done *in situ* on the specimen. The system in this configuration was found to offer very good flexibility and ease of alignment.

2.3 Theory of PTM

The configuration of the photon-tunneling microscope was based on an Olympus BX40 main frame. The CCD was used in place of the photo detector to take the optical signal. Placing a few drops of oil between the oil objective and the transducer led to a condition of the total internal reflection (TIR). The transducer serves as the reference plane of the total internal reflection. During operations, the reference plane is placed on top of the specimen. Converting the gray-scaled image with respect to the reference plane leads to a real time surface profile measurement with nanometer vertical height resolution. As illustrated in Fig. 2, no scanning source or detector was needed to construct the system. The newly developed system adopts a halogen lamp as the illumination source, a CCD for image grabbing, and a reflection type oil immersion objective of numerical aperture 1.3 and 100 \times magnification to achieve the frustrated total internal reflection (FTIR). In the experimental set-up, a 0.17mm microscope cover glass served as the PTM transducer. The oil was placed between the cover glass

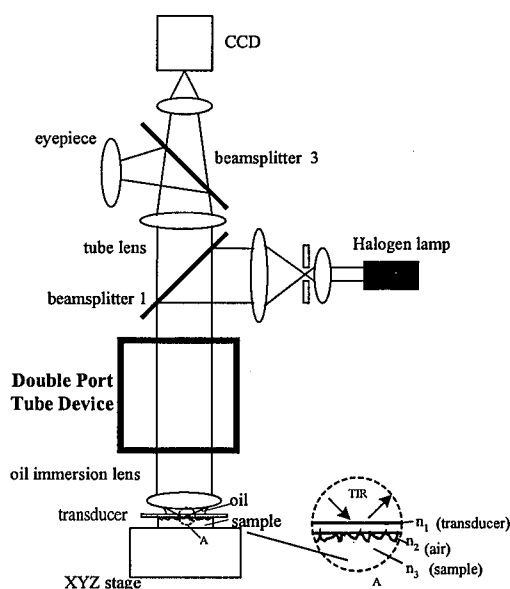


Fig. 2 Schematic of the TIR in the PTM

and the oil immersion objective. The sample was placed beneath the cover glass. Since no oil was used between the sample and the cover glass, a TIR phenomenon (Fig. 2) appeared at the interface between the cover glass and the sample. That is, the underside of the cover glass acted as the photon-tunneling interface. The sample surface of interest was positioned coplanar with the object plane. Only the annular portion of the incident light beam, whose intensity distribution was used to illuminate the sample, resulted in the effect of total internal reflection. The amount of intensity decay of the evanescent waves depends on the distance between the bottom side of the cover glass and the optical property of the sample that is brought to within the photon tunneling distance (typically $1/4 \lambda$) of the photon-tunneling interface. Each pixel in the CCD collects the intensity reflected from the corresponding spot of the sample, which forms a massive array of optical probes that operate simultaneously in parallel for real-time imaging. The decay of evanescent field amplitude with distance from the boundary is given by [13]

$$I = I_0 \exp(-z/z_0) \quad (1)$$

where z_0 is the effective transmission depth and I_0 is the magnitude of the light beam at the interface of Medium 1 and Medium 2. The optical refractive indices of these two media are n_1 and n_2 , respectively. It is clear from Eq. (1) that I is a function of z and one can compute z from the measured reflective intensity I . The above equation illustrates that there is a moving-waveform along the direction between the photon-tunneling interface and the top surface of the sample (Fig. 2), but its magnitude decreases exponentially as the field is an evanescent field. When there is an additional medium with refractive index $n_3 > n_2$, the wave will continue to propagate through Medium 3.

The frustrated total internal reflection (FTIR) phenomenon in which the photon tunneling microscopy was based will be present. Therefore, if the surface of Medium 3 has a lateral or longitudinal variation and Medium 3 is an isotropic homogeneous optical material, the reflected wave in the interface of Medium 1 and Medium 2 will change correspondingly. A linear change in the separation z causes an inverse and exponential change in the energy transfer. When the distance increases, the intensity of the gray scale image decreases, and vice versa. By measuring the variation of the intensity of the reflected waves during operation, the CCD can grab the gray-scale images of the specimen surface profile.

2.4 Integrated measurement and calibration

Different measurement ranges can be investigated by using the two functions of this newly developed microscope system. Comparing the axial resolution of PTM and CLSM, we can see clearly that the former is better than the later as shown in Fig. 3. The response curve of the PTM was obtained by Eq. (1) and that of the CLSM was obtained by [13],

$$I \propto \left\{ \frac{\sin [kz(1 - \cos \alpha)]}{kz(1 - \cos \alpha)} \right\}^2 \quad (2)$$

which depends on the aperture angle α of the microscope objective, the wavelength of light λ , the wavenumber $k = 2\pi/\lambda$, and the coordinate of defocusing z . The PTM can measure the full-field area, which is a $40\mu\text{m}$ by $40\mu\text{m}$ area, and achieves basically real-time imaging capability. In comparison, the XY stage used in the confocal system for sample traversing scans only a $15\mu\text{m}$ by $15\mu\text{m}$ area, but which can certainly be expanded by a larger stage, and thus determines the maximum scanning range of the CLSM portion of this system. The oil objective was aligned so as to grab the wide sample image first. Without moving the sample

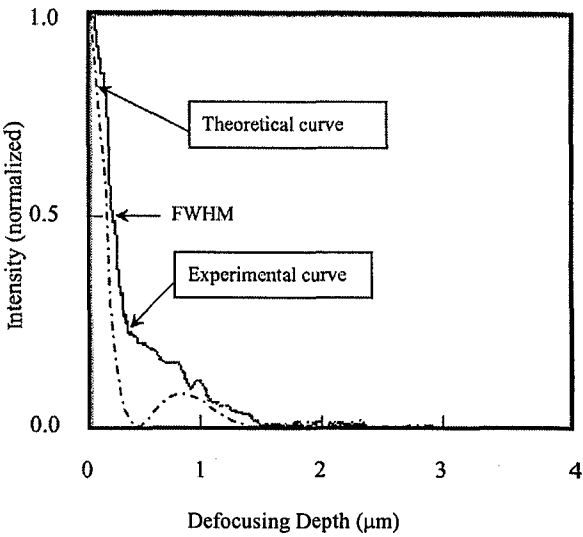


Fig. 4 The measured depth response of the CLSM using a 100x at NA = 0.8 objective in air at $\lambda = 635\text{nm}$

on the stage, the objective of magnification ratio 100x and NA = 0.8 was next adopted to implement CLSM to measure the smaller area near the micro-mirror tip. The depth resolution in terms of a full width half maximum (FWHM) in the confocal system is shown in Fig. 4, which was obtained by measuring a flat mirror as the calibration specimen. The results of the experimental depth response and theoretical curve are approximations [13] except for the noise at the defocusing points.

To calibrate the system performance, the profile of a commercially available diffraction grating was scanned topographically. The grating profile was measured to have a height of 155nm and spatial frequency of 600 lines/mm ($1.67\mu\text{m}$ grating pitch), which agrees well with the specifications of this grating. Figures 5(a) and 5(b) show the data measured by the CLSM and AFM respectively. Comparing the calibration results, the newly developed system can accurately determine the shape of the grating. Furthermore, the data indicates that the system possesses accuracy in the range of $\pm 5\text{nm}$ for overall ranges of 200nm. For overall measurement ranges of 200 to 1500nm, the resolution was found to be $\pm 20\text{nm}$. Figure 5(c) shows that the measurement results obtained by the CLSM and AFM. The results obtained demonstrate that these two methods agree well with respect to each other except at the tips of the grating. This slight discrepancy can be attributed to the fact that the lateral resolution of a CLSM is less than that of an AFM. More specifically, the difference in lateral resolution makes the grating profile measured with the CLSM appear smoother than that measured by the AFM.

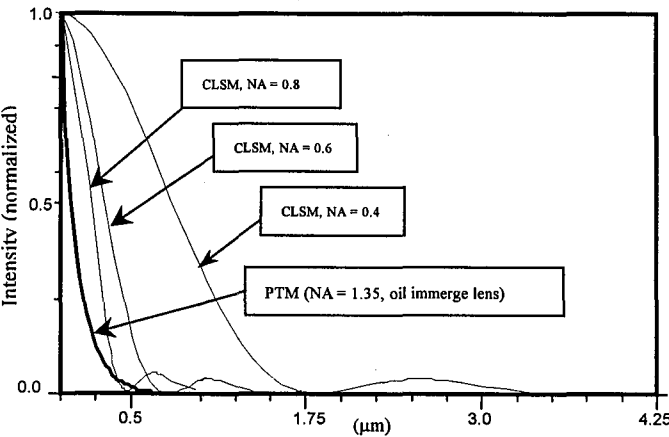


Fig. 3 The different ranges measured between the CLSM (NA = 0.4, 0.6, and 0.8) and PTM (NA = 1.35)

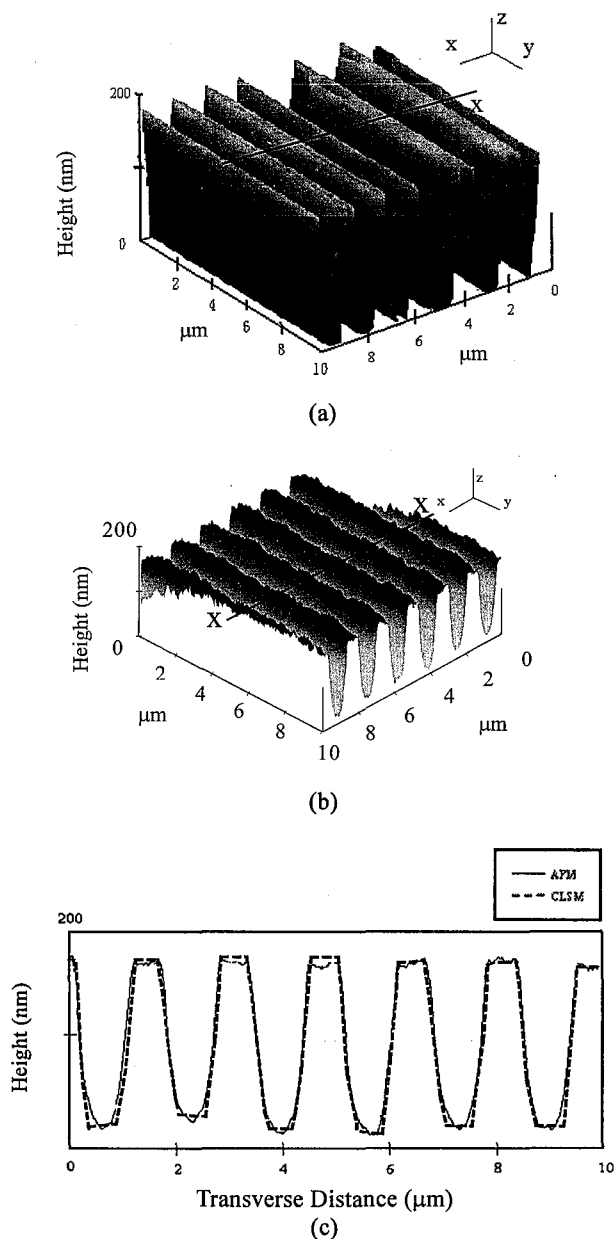


Fig. 5 Profile of a grating of $1.667\mu\text{m}$ pitch as measured by (a) CLSM (b) AFM, and (c) compared along the x-x section

3. SPECIMEN PREPARATIONS AND LOADING

The specimen of interest was a micro-mirror, which was driven by a micro-actuator made of Ni, Au and silicon substrate [14~17]. The top and bottom electrodes were made from the same wafer in order to facilitate the gap control of the two electrodes. The main fabrication processes are (1) a lift off of a 200 angstrom thick Cr and 1000 angstrom thick Au, (2) dry and wet etching steps, (3) anodic bonding with operating temperature higher than 400°C and operating voltage between 350 and 500V. The specimen used is shown in Figs. 6 and 7(a), which is a newly fabricated $700\mu\text{m}$ by $700\mu\text{m}$ torsional micro-mirror suspended on a $10\mu\text{m}$ high \times $4\mu\text{m}$ wide

beam. The distance between the doped polysilicon mirror and the bottom electrode (the silicon substrate) is about $10\mu\text{m}$ (Figs. 6 and 7). The specimen was loaded by applying external voltage to the two electrodes, which created a bending moment and a torque to induce a rotation angle at the micro-mirror. When the externally applied electrical potential reached a level of 30V, the substrate began to suspend. The substrate was covered by a 300nm thick Si_3N_4 , which served as the electrically insulating layer to protect the device from short-circuiting. As the length and width of the micro-mirror were much longer than its thickness, the deformation of the micro-mirror surface itself was neglected.

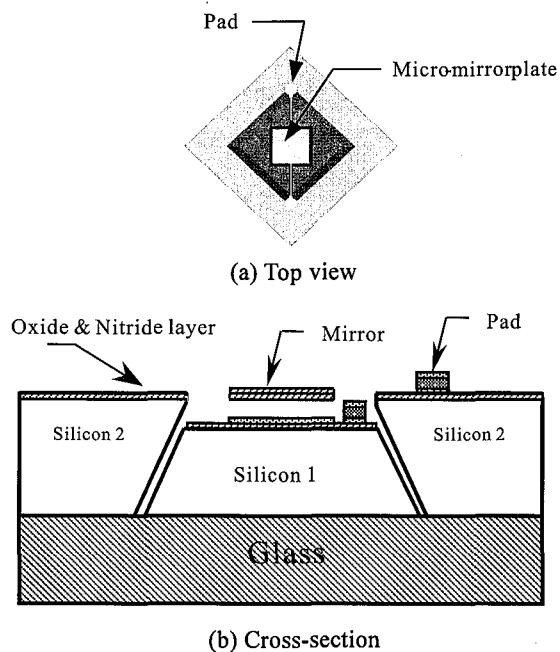


Fig. 6 Microstructure of the specimen from (a) top view and (b) cross-section

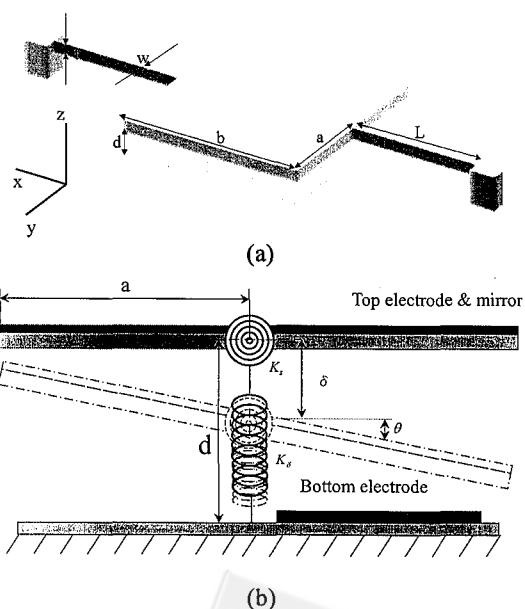


Fig. 7 Schematic of the interest specimen: (a) 3D configuration and (b) mechanical model

4. ANALYSIS OF ELECTROSTATIC DEFLECTION

The electrostatic field theory [18], which treats an electro-statically deflectable micro-mirror as a charged-plate capacitor with an upper plate suspended by a spring was adopted (Fig. 7(b)). The equivalent capacitance of the capacitor connected in the series can be expressed as $C = C_2 = \epsilon_0 A/g$ (Fig. 8), where C is the total capacitance and C_2 is the equivalent capacitance created by the air gap. Consequently, the electrical force F_e acting on the upper electrode can be shown to be

$$F_e = \frac{\epsilon_0 A V^2}{2g^2} \quad (3)$$

where A is the plate area, g is the distance between both plates, V is the applied electric voltage, and $\epsilon_0 = 8.85 \times 10^{-12}$ F/m is the vacuum permittivity. The total electric torque T_e acting on the mirror element can be calculated by

$$T_e = \int_0^a F_e \cdot y \cdot dy \quad (4)$$

where a is the width of the address electrode. Performing simple geometry calculations, it is clear that once the mirror is rotated by an angle δ , the electrode gap can be expressed as $g = d - \delta - y \cdot \tan \theta$, where δ is deformation of each beam where the geometry model can be seen in Fig. 9 and d is the initial gap between the mirror and the corresponding addressing electrode. The mechanical model of the micro-mirror can be seen in Fig. 9. The rotation angle of the micro-mirror θ with respect to the external voltage is shown in Fig. 10. From Eqs. (3) and (4), an expression for the electric torque T_e can be found as:

$$T_e = \int_0^a \frac{\epsilon_0 b V^2 y}{2(d - \delta - y \tan \theta)^2} dy$$

$$= \frac{\epsilon_0 b V^2}{2 \tan^2 \theta} \left[\ln \left(1 - \frac{a}{d - \delta} \tan \theta \right) + \frac{1}{1 - \frac{a}{d - \delta} \tan \theta} - 1 \right] \quad (5)$$

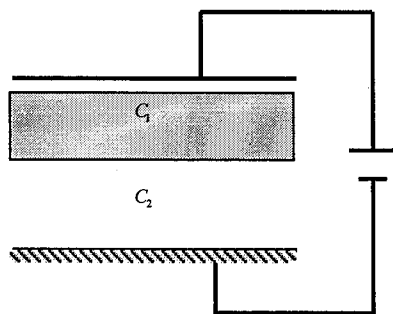


Fig. 8 Model of a plate capacitor

where b is the length of the electrode. For small rotations, Eq. (5) can be expanded by using the Taylor's series in order to arrive at the approximation formula

$$T_e = \frac{b \epsilon_0 a^2 V^2}{4(d - \delta)^2} \quad (6)$$

From Eq. (6), the torque is proportional to the electrode length b and is inversely proportional to the square of the electrode separation d . For numerical calculations, a torsional micro-mirror with an addressing electrode of $350 \mu\text{m}$ by $700 \mu\text{m}$ was assumed and the electrode gap d was set at $25 \mu\text{m}$. The mechanical torque T_m , which was created by the torsional suspension spring, counteracts the electrically induced torque T_e . The magnitude of the mechanical torque depends on the geometry and material properties of the beams while the relationship between V and θ can be calculated by using the following formulas

$$F_m = K_\delta \cdot \delta \quad (7)$$

where F_m is the spring force resulting from the electrostatic force, $K_\delta = 24EI/L^3$ with E and I as the effective Young's modulus and the moment of inertia of the supporting beam on the side of the mirror plate respectively, I is the bending stiffness of a supported beam, δ is deformation of each beam, and the geometry model can be seen in Fig. 9. The mechanical torque resulting from δ is

$$T_m = K_s \cdot \theta = \left(2 \cdot \frac{G \cdot J}{L} \right) \cdot \theta \quad (8)$$

where L is the length of the torsional spring, G is the torsion modulus, J is the polar moment of inertia, and $K_s = 2GJ/L$ is the torsional stiffness of the spring. Even though the material was created by a MEMS process and may not be pure polysilicon, it was assumed to be pure polysilicon and the material constants used were taken directly from the data book.

$$C = C_1 \square C_2$$

$$C = \frac{C_1 C_2}{C_1 + C_2}$$

$$C_1 = \epsilon_1 \frac{A}{g_1}$$

$$C_2 = \epsilon_2 \frac{A}{g_2}$$

$$\text{if } C_1 \square C_2$$

$$\text{then } C = \frac{C_1 C_2}{C_1 + C_2} = \frac{C_2}{1 + \frac{C_2}{C_1}} \approx C_2$$

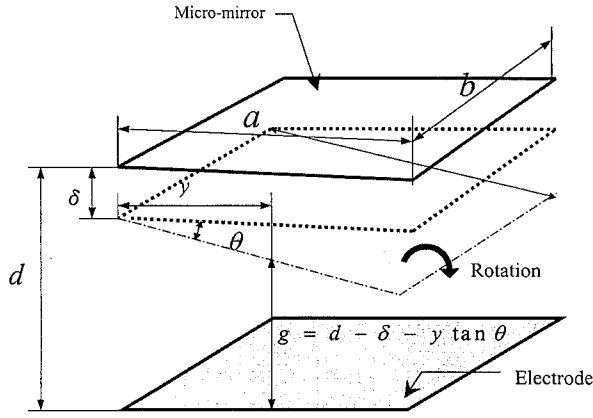


Fig. 9 Geometry of the micro-mirror

The torsion bars used for the numerical calculations had a length l of $500\mu\text{m}$ and a cross-section of $4\mu\text{m}$ wide and $10\mu\text{m}$ high. The torsional moment of inertia for the beams with a rectangular cross-section (width w and thickness t) is [19]:

$$J = \frac{1}{3} wt^3 \cdot \left[1 - \frac{192t}{\pi^5 w} \tanh\left(\frac{\pi w}{2t}\right) \right] \quad (9)$$

for $t \geq w$

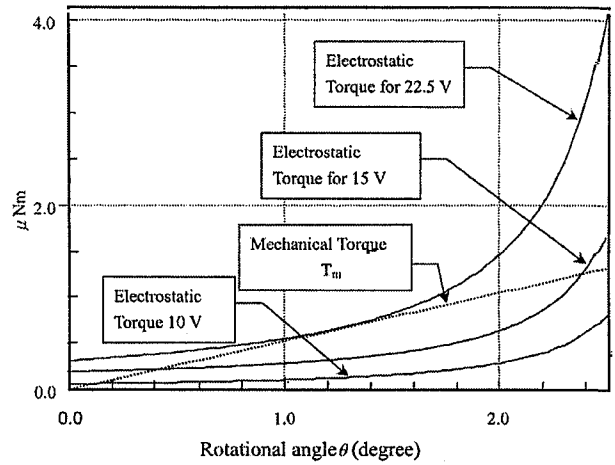
With the dimensions of the torsion micro-mirror, the polar moment of inertia J of the micro-mirror can be calculated to be $1.467 \times 10^{-21} \text{m}^4$. The mechanical torque per degree of twist T_m/θ can then be derived by substituting J into Eq. (8). From Eqs. (8) and (9), it can be deduced that the torsional moment of the mirror is inversely proportional to the length and is directly proportional to the width and to the third power of the thickness of the beams (for $t \gg w$). The electromechanical performance of the torsional mirror can be roughly predicted by using the electric torque T_e as calculated above. Employing Eqs. (4) and (5), the voltage and the angle of abrupt tilting can be calculated. Finally, we can obtain the general form of the torque of spring K_s

$$T_m = 2 \cdot G \frac{\left\{ \frac{1}{3} \left[1 - \frac{192t}{\pi^5 w} \tanh\left(\frac{\pi w}{2t}\right) \right] wt^3 \right\}}{L} \cdot \theta \quad (10)$$

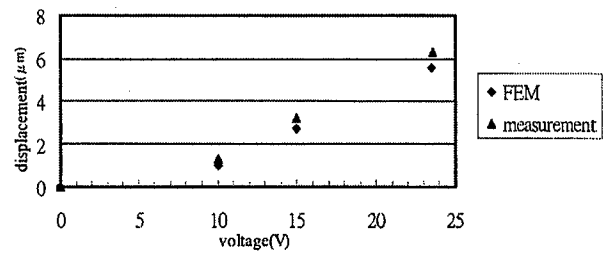
The distance y at different voltages can be determined by balancing the electrical and mechanical forces, i.e., set $T_e = T_m$ in Eq. (10) leading to

$$T_m = \frac{\epsilon_0 b V^2}{2 \tan^2 \theta} \left[\ln\left(1 - \frac{a}{d-\delta} \tan \theta\right) + \frac{1}{1 - \frac{a}{d-\delta} \tan \theta} - 1 \right] \quad (11)$$

The relationship between V and θ can be calculated from Eq. (11) and the analytical results are shown in



(a)



(b)

Fig. 10 (a) Torque T_s vs. rotational angle for a micro-mirror with external voltage using theoretical analysis and (b) simulated and measured results of the plate capacitor

Fig. 10(a). By using this formula, the external voltage and the twist angle can be computed by substituting all related numerical conditions into the equation. The slope of the characteristic curve can be increased drastically when the mirror plate becomes very sensitive to the variations in the driving voltage. In fact, once the driving voltage reaches a critical value, which is $V_c = 22.5\text{V}$ in our case, then

$$V(q) = \sqrt{\frac{2 \cdot G \frac{\left\{ \frac{1}{3} \left[1 - \frac{192t}{\pi^5 w} \tanh\left(\frac{\pi w}{2t}\right) \right] wt^3 \right\}}{L} \cdot \theta}{\frac{\epsilon_0 b}{2} \left[\csc^2 \theta \cdot \ln\left(1 - \frac{a}{d-\delta} \tan \theta\right) + \frac{\frac{a}{d} \sec^2 \theta}{\tan \theta \cdot \left(1 - \frac{a}{d-\delta} \tan \theta\right)} \right]}} \quad (12)$$

The plate will then experience an abrupt tilting until it contacts the substrate. It should be noted that the critical point $\theta = 1.21^\circ$ (i.e. unstable point) cannot be used to estimate the twist angle once θ approaches beyond this point.

5. RESULTS OF THE FEM CALCULATIONS AND EXPERIMENTS

From Section 4, a FEM model of a plate capacitor established according to Fig. 7(a) was developed to pursue simulations of the analytical solutions. Figure 10(a) shows the calculated distances of the upper plate of the capacitor if the applied voltages are set at 0V, 10V, 15V, and 22.5V. The pull-in voltage calculated by the FEM model was 23.5V. The slight discrepancy between the pull-in voltage predicted by the analytical model at 22.5V and by the FEM model at 23.5V can be attributed to the change of the electrostatic force distribution in the analytical model different from that in the FEM model. The twist angle of the torsional micro-mirror (Fig. 7(b)) is demonstrated in Fig. 10(a). The data points shown in Fig. 10(b) were calculated by using the above-described FEM. The measured pull-in voltage was about 27.5V, which was obtained by increasing the applied voltage gradually from the condition at zero V. It is clear that this data is slightly different from the 23.5V simulated value. The discrepancies between the simulation and the measurement results can be attributed to the imperfect fabrications of the micro-mirror. It should be noted that it is very difficult to measure the profile or deformation of the micro-mirror when the pull-in voltage reaches the critical point, as the system is unstable beyond the pull-in voltage.

As described above, the size of the micro-mirror was $700\mu\text{m}$ by $700\mu\text{m}$ (i.e. $2a = 700\mu\text{m}$, $b = 700\mu\text{m}$ as shown in Fig. 9), and the externally applied voltage was at 0V, 10V, 15V, and 22.5V. In the FEM calculation, the out-of-plane deformation at the maximum micro-mirror tip was $0\mu\text{m}$, $0.99\mu\text{m}$, $2.68\mu\text{m}$, and $5.53\mu\text{m}$.

Figure 11(a) displays the un-deformed micro-mirror measured by PTM. As the PTM can measure wide and real-time imaging area, the profile of $40\mu\text{m}$ by $40\mu\text{m}$ area was imaged by using the PTM. The maximum peak to valley surface roughness R_{max} was about 150 nm . As the total metrology area of the current CLSM was around $15\mu\text{m}$ by $15\mu\text{m}$ due to the travel range of the scanning stage used, a sub-area of the above-mentioned $40\mu\text{m}$ by $40\mu\text{m}$ area was chosen to perform the CLSM measurement. With the intention to measure the detailed profile and the maximum displacement, the $15\mu\text{m}$ by $15\mu\text{m}$ scanning area was chosen near the micro-mirror tips. Before the driving voltage was applied, the surface roughness R_{max} was measured to be 483.11 nm in the AFM (Fig. 11(b)) and the corresponding measurement performed by the CLSM was 466 nm (Fig. 11(c)).

Figure 12 shows the comparisons between the FEM and the experimental data. The FEM predicted that the

maximum displacement value would be $0.99\mu\text{m}$ at a 10V externally applied voltage. Similarly, $2.68\mu\text{m}$ was obtained at 15V and $5.53\mu\text{m}$ at 23.5V. On the other hand, the measured values were about $1.2\mu\text{m}$ at 10V, $3.4\mu\text{m}$ at 15V, and $6.6\mu\text{m}$ at 23.5V, respectively. The rotational angles predicted by the FEM were 0.16° at 10V, 0.43° at 15V, and 0.905° at 23.5V. In comparison, the measured rotational angles were 0.2° at 10V, 0.56° at 15V, and 1.28° at 23.5V. Apparently, the results predicted by using the FEM and by using the analytical models are reasonably close. However, the FEM results do not agree very well with the

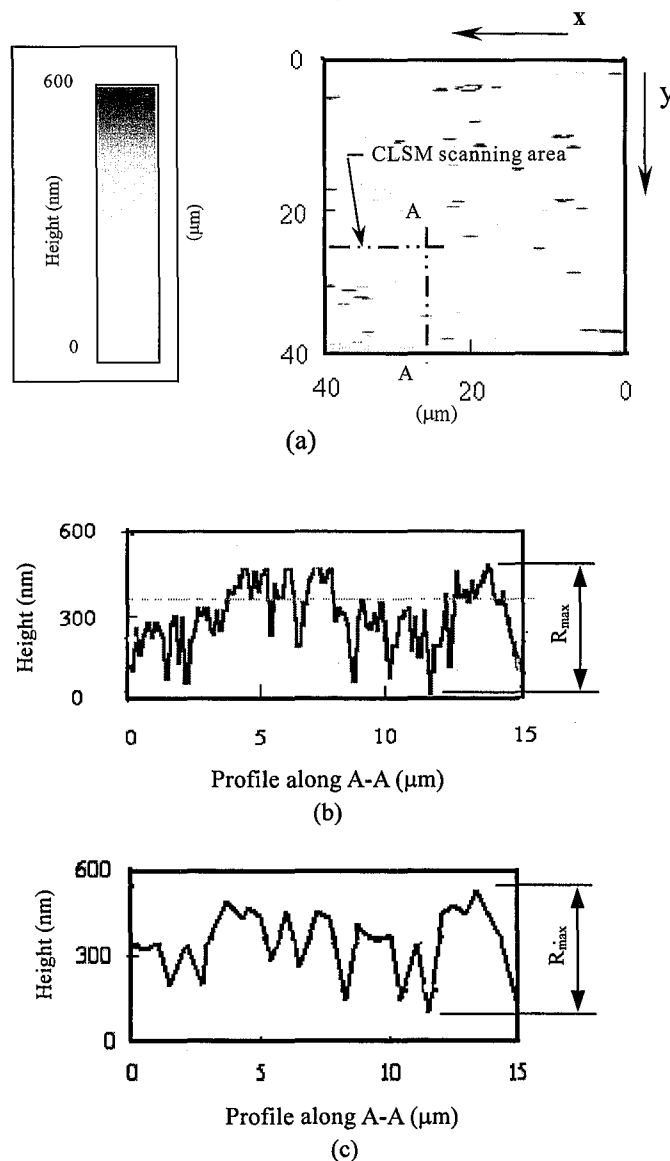


Fig. 11 A $40\mu\text{m}$ by $40\mu\text{m}$ measured area was located on the micromirror surface before deformation: (a) 3D profile measured by PTM with $R_{\text{ams}} = 466\text{ nm}$, (b) surface roughness along the AA-section measured by the AFM with $R_{\text{ams}} = 483.11\text{ nm}$ and (c) surface roughness along the AA-section measured by the CLSM

experimental results. The main reason can be attributed to the surface roughness and the imperfect constructions of the geometry of the micro-mirrors fabricated as shown in Fig. 11(b). In addition, the MEMS structure was assumed to have a rigid boundary condition in the FEM model. On the other hand, the experiments were actually performed on MEMS fabricated micromirrors with deflectable boundaries. The roughness of the undeformed micromirror is almost of the same order as that the deformation predicted by the FEM. This roughness is non-negligible when measuring the real deformation in different applied voltages (Fig. 11(a) and Fig. 12). In addition, the displacement δ initially equals to 0 at the mechanical model. By using force balance $F_m = F_e$, the displacement predicted by the FEM are $0.1\mu\text{m}$, $0.2\mu\text{m}$, and $0.4\mu\text{m}$ when the applied voltage are 10V, 15V and 23.5V, respectively. In comparison, the experimentally obtained displacements are $0.16\mu\text{m}$, $0.29\mu\text{m}$, and $0.75\mu\text{m}$ at the corresponding driving voltages. It is quite clear that the FEM results in these cases are smaller than the measured values.

Figure 13 displays the 3D profile as measured by using the CLSM. Increasing the applied voltage, the deformation will increase gradually. When the applied voltage reaches 10V, the maximum deformation and rotational angle will still be very small (Fig. 13(a)). This is due to the fact that the electrostatic force needs to overcome a mechanical force F_m and the initial deformation is not apparent. Once the disparity between T_m and T_e widens, the distortion becomes more serious. Figures 13(b) and 13(c) show the experimental results when the externally applied voltages are set at 15V and 23.5V. According to the description in Sec. 4, the deformation and the twist angle can be increased non-linearly when the applied voltage is raised. These experiments confirm that the theoretical analysis indeed provides some valuable and accurate results.

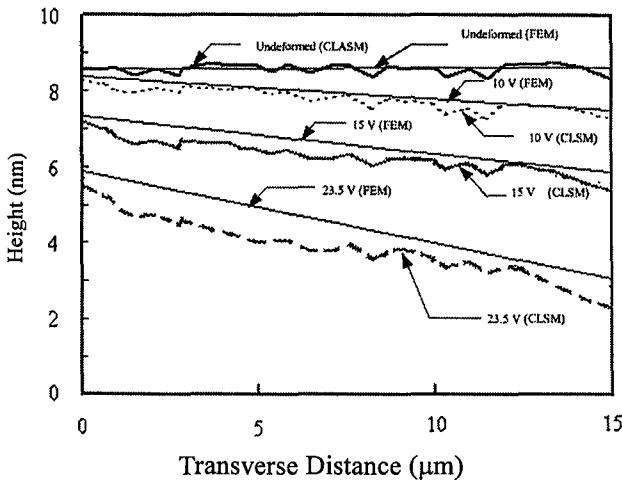


Fig. 12 Two-dimensional profile obtained by FEM and CLSM

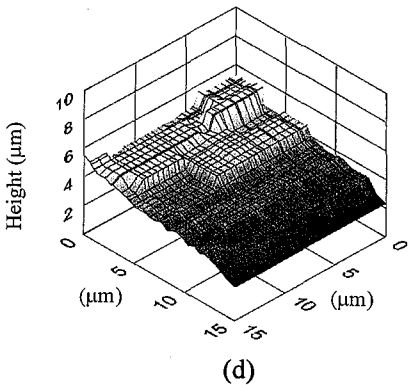
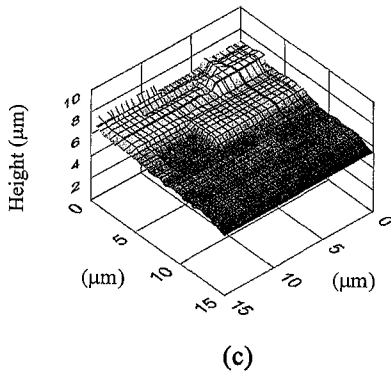
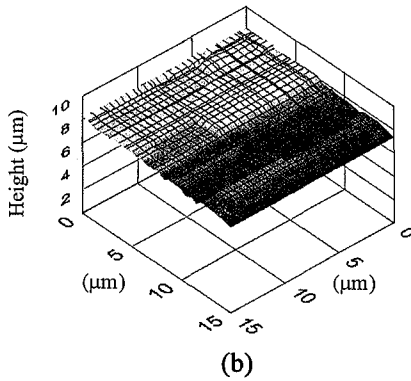
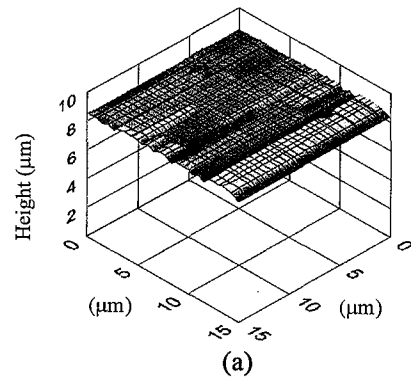


Fig. 13 Three-dimensional profile of the deformed micro-mirror measured by the CLSM: (a) before deformation and when the externally applied voltages are (b) 10V, (c) 15V, and (d) 23.5V respectively

6. DISCUSSIONS AND CONCLUSIONS

This paper presents a newly developed optical system, which is based on a confocal laser scanning microscope and a photon-tunneling microscope. Since the photon-tunneling microscope can perform full field measurement and the confocal laser scanning microscope is good for point-by-point measurements, the two sub-systems of this newly developed microscope are complimentary to each other. These same complimentary characteristics extend to the dynamic range and resolution. The design and the implementation of the photon-tunneling microscope and the confocal scanning laser microscope are detailed. Several conclusions can be drawn based on the experimental data obtained. This newly developed optical system can be used to measure the three-dimensional profile and displacement of a micro-mirror easily and in a short amount of time, i.e., it can provide a non-destructive evaluation method to retrieve surface profiles of micro-systems. As microscopic resolution depends on the numerical aperture of a microscope objective, one can obtain a more superior resolution by using a microscope of a higher numerical aperture. In other words, surface roughness of various orders can be measured by adopting objectives of different magnifications and different numerical apertures.

The experimental results show that the micro-machined mirror is distorted even before the voltage is applied externally. This deformation can be attributed to the residual stresses induced by the thermal oxide. The reason lies on the fact that the micro-machined mirror was fabricated by removing the mirror's supporting substrate, which removed the traction at the interface of the mirror-substrate as well. With the traction removed, the structure becomes free to deform at the out-of-plane direction, and is thus distorted in the out-of-plane deformation direction. This pre-distortion was not accounted for in the analytical solution and the finite element method computation, which caused the discrepancy between the experimental results and the theoretical results. In addition, the noise induced by the surface roughness of the micro-mirror further increases the discrepancy between the experimental results and the theoretical predictions. With the complimentary capabilities, resolutions, and dynamic ranges of the confocal scanning laser microscope and the photon-tunneling microscope, the newly developed system is shown to be versatile and useful in characterizing the performance of various micro-electrical systems.

REFERENCES

[1] Chu, W. H., Mehregany, M. and Mullen, B. H., "Analysis of tip deflection and force a bimetallic microactuator," *J. Micromech. Microeng.*, 3, pp. 4-7 (1993).
 [2] Chung, S. W. and Kim, Y. K., "Design and

fabrication of 10×10 micro-apatial light modulator array for phase and amplitude modulation," *Sens. Actuators A*, 78(1), pp. 63-70 (1999).
 [3] Krishnamoorthy, U., Li, K., Yu, K., Lee, D., Heritage, J. P. and Solgaard, O., "Dual-mode micromirrors for optical phased array applications," *Sens. Actuators A*, 97-98, pp. 21-26 (2002).
 [4] Buhler, J., Funk, J., Korvink, J. G., Steiner, F. P., Sarro, P. M. and Baltes, H., "A silicon resonant sensor structure for Coriolis mass-flow measurements," *J. Microelectromech. Syst.*, 6(2), pp. 126-135 (1997).
 [5] Zavracky, P. M., Majumber, S. and McGruer, E., "Micromechanical switches fabricated using nickel surface micromachining," *J. Microelectromech. Syst.*, 6(1), pp. 3-9 (1997).
 [6] Strozewski, K. J., Wang, C. Y., Wetsel Jr., G. C., Boysel Jr., R. M. and Florence Jr., J. M., "Optical power induced damage to microelectromechanical mirrors," *J. Appl. Phys.*, 73, pp. 7125-7128 (1993).
 [7] Chung, S. W., Shin, J. W., Kim, Y. K. and Han, B. S., "Design and fabrication of micromirror supported by electroplated nickel posts," *Sens. Actuators A*, 54(1-3), pp. 464-467 (1996).
 [8] Min, Y.-H. and Kim, Y.-K., "Modeling, design, fabrication and measurement of a single layer polysilicon micro-mirror with initial curvature compensation," *Sens. Actuators A*, 78(1), pp. 8-17 (1999).
 [9] Fischer, M., Giousouf, M., Schaepperle, J., Eichner, D., Weinmann, M., von Munch, W. and Assmus, F., "Electrostatically deflectable polysilicon micromirrors-dynamic behaviour and comparison with the results from FEM modeling with ANSYS," *Sens. Actuators A*, 67(1-3), pp. 89-95 (1998).
 [10] Degani, O., Socher, E., Lipson, A., Leitner, T., Setter, D. J., Kaldor, S. and Nemirovsky, Y., "Pull-in study of an electrostatic torsion microactuator," *J. Microelectromech. Syst.*, 7(4), pp. 373-379 (1998).
 [11] Shin, J. W., Chung, S. W., Kim, Y. K. and Choi, B. K., "Silicon mirror arrays fabricated by using bulk- and surface micromachining," *Sens. Actuators A*, 66(1-3), pp. 144-149 (1998).
 [12] Guerra, J. M., "Photon tunneling microscopy," *Applied Optics*, 29(26), pp. 3741-3752 (1990).
 [13] Wilson, T. and Sheppard, C. J. R., *Theory and Practice of Scanning Optical Microscopy*, Academic Press, London, UK (1984).
 [14] Fang, W. and Wickert, J. A., "Determining mean and gradient residual stresses in thin films using micromachined cantilevers," *J. Micromech.*

- Microeng.*, 6, pp. 301–309 (1996).
- [15] Fang, W. and Wickert, J. A., “Comments on measuring thin-film stresses using bilayer micromachined beams,” *J. Micromech. Microeng.*, 5, pp. 276–281(1995).
- [16] Chu, T. C., Ranson, W. F., Sutton, M. A. and Peters, W. H., “Applications of digital image-correlation techniques to experimental mechanics,” *Experimental Mechanics*, 25(3), pp. 232–244 (1985).
- [17] Meng, Q., Mehregany, M. and Mullen, R. L., “Theoretical modeling of microfabricated beams with elastically restrained supports,” *J. Micro-electromechanical System*, 2(2), pp. 128–137 (1993).
- [18] Cheng, D. K., *Field and Wave Electromagnetics*, Addison Wesley, Longman, CO, USA (1996).
- [19] Timoshenko, S. P. and Goodier, J. N., *Theory of Elasticity*, 3rd ed., McGraw-Hill, New York, New York, USA (1970).

(Manuscript received July 30, 2002,
Accepted for publication Sept. 26, 2002.)